Article

Evaluation of the Biodistribution of Serinolamide-Derivatized C_{60} Fullerene

Nicholas G. Zaibaq [1,†] ⓘ, **Alyssa C. Pollard** [1,2,†], **Michael J. Collins** [1,‡], **Federica Pisaneschi** [2] ⓘ, **Mark D. Pagel** [1,2,*] **and Lon J. Wilson** [1,*]

1   Department of Chemistry and Smalley-Curl Institute, Rice University, 6100 Main St, Houston, TX 77005, USA; zaibaqn@gmail.com (N.G.Z.); acp4@rice.edu (A.C.P.); mjc178@pitt.edu (M.J.C.)
2   Department of Cancer Systems Imaging, MD Anderson Cancer Center, 1881 East Rd, Houston, TX 77054, USA; fpisaneschi@mdanderson.org
*   Correspondence: mdpagel@mdanderson.org (M.D.P.); durango@rice.edu (L.J.W.); Tel.: +202-(713)-205-8515 (M.D.P.); +202-(713)-348-3476 (L.J.W.)
†   These authors contributed equally to this work.
‡   Present Address: Department of Chemistry, University of Pittsburgh, 3960 Forbes Ave, Pittsburgh, PA 15260, USA.

Abstract: Carbon nanoparticles have consistently been of great interest in medicine. However, there are currently no clinical materials based on carbon nanoparticles, due to inconsistent biodistribution and excretion data. In this work, we have synthesized a novel C_{60} derivative with a metal chelating agent (1,4,7-Triazacyclononane-1,4,7-triacetic acid; NOTA) covalently bound to the C_{60} cage and radiolabeled with copper-64 ($t_{1/2}$ = 12.7 h). Biodistribution of the material was assessed in vivo using positron emission tomography (PET). Bingel-Hirsch chemistry was employed to functionalize the fullerene cage with highly water-soluble serinolamide groups allowing this new C_{60} conjugate to clear quickly from mice almost exclusively through the kidneys. Comparing the present results to the larger context of reports of biocompatible fullerene derivatives, this work offers an important evaluation of the in vivo biodistribution, using experimental evidence to establish functionalization guidelines for future C_{60}-based biomedical platforms.

Keywords: fullerene; serinolamide; biodistribution; pharmacokinetics; PET

1. Introduction

Recently, nanoparticles such as silicon nanoparticles [1], superparamagnetic iron oxide nanoparticles [2], and carbon nanotubes [3–5] have been studied extensively for biomedical applications as they constitute a promising platform upon which therapeutic, imaging, and/or targeting agents can be loaded [6–8]. Specifically, C_{60} fullerene shows promise for biomedical applications because this multi-functional platform also has a variety of inherent advantages [9]. C_{60} is chemically versatile, and many synthetic strategies of derivatization have already been developed [10–16], which provides great flexibility when designing a C_{60} engrafted with therapeutics. Inherently, C_{60} has also shown strong antioxidant behavior through its ability to quench free radicals [17,18] and has been observed to nearly double the lifespan of rodents, presumably because of this radical-scavenging property [19,20]. Conversely, certain C_{60} derivatives can generate reactive oxygen species under light irradiation, allowing these derivatives to be used for photodynamic therapy (PDT) against cancer [21,22]. Furthermore, C_{60} can be chemically decorated with molecular targeting agents [23,24], imaging agents [25–27], and anticancer drugs [24,28–31] to be used as a therapeutic delivery vector, a diagnostic agent, or a combination of the two (known as a theranostic agent).

Due to these advantageous properties of C_{60}, we were inspired to design a platform that could be used as drug delivery system, to explore the potential of C_{60} as a multimodal therapeutic agent. We chose to functionalize C_{60} with the serinolamide moiety used to solubilize clinical iodobenzene X-ray contrast agents [32]. In a compound called C_{60}-serinol, six malonate groups containing these serinolamide moieties surround the fullerene core in an octahedral arrangement (Figure 1, left), which affords the material with high water solubility and low cytotoxicity, making it a desirable starting material for further functionalization [33–35]. Like other hexakisadducts of C_{60}, C_{60}-serinol is monoisomeric, which helps to ensure a low polydispersity index that is necessary for clinical translation. C_{60}-serinol materials have been shown to pass through the nuclear membranes of liver cancer cells [34] and has been used to deliver DNA to mouse fibroblasts and marrow stromal cells [36]. In addition, when derivatized with paclitaxel, C_{60}-serinol can kill cancer cells in vivo without producing the weight loss associated with other formulations [37]. These results demonstrate C_{60}-serinol's potential to serve as a drug delivery platform, as well as the potential to meliorate the negative side effects of chemotherapy.
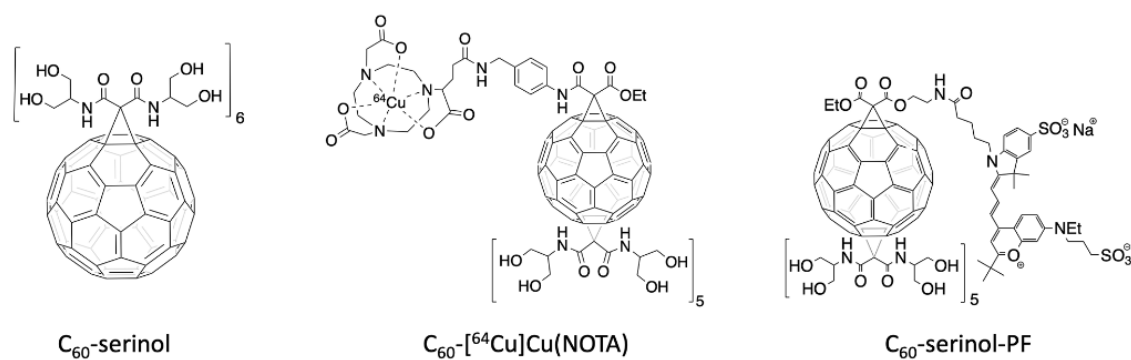

Figure 1. Structure of the C_{60}-serinol (left). Structure of the radioactive C_{60}-NOTA conjugate, radiolabeled with copper-64 (C_{60}-[^{64}Cu]Cu(NOTA), middle). Structure of the fluorescently-labeled C_{60}-serinol conjugate with PromoFluor 633 (C_{60}-serinol-PF, right).

An important aspect of designing drug delivery platforms is the study of the biodistribution and excretion profile of the compound. Thus far, the biodistribution profiles of C_{60} reported in the literature, including C_{60}-serinol, are discordant [38–41]. This work aims to reevaluate the in vivo behavior of this nanomaterial non-invasively, using the imaging technique positron emission tomography (PET). Understanding how C_{60}-serinol behaves in vivo is a valuable step toward developing C_{60}-derived materials for biomedical applications.

PET is routinely used in the clinic and can image whole organisms non-invasively with high sensitivity that accurately quantifies the distribution of the radioactive radiopharmaceutical in various organs. Of the many radionuclides currently used for PET imaging, we have employed copper-64 because of its relatively low cost and long 12.7 h half-life, which permits imaging at later time points post-injection [42,43]. To chelate copper-64 for radiolabeling C_{60}, we have synthesized a C_{60}-serinol derivative (Figure 1, center), with five malonates carrying serinolamide groups and a covalently linked NOTA chelate. [^{64}Cu]Cu(NOTA) has been shown to be stable under biological conditions [44]. The biodistribution data of C_{60}-[^{64}Cu]Cu(NOTA), collected herein by PET, are then compared to our previously reported data of fluorescently-labeled C_{60}-serinol (C_{60}-serinol-PF, Figure 1, right), as well as other C_{60} derivatives reported in the literature.

2. Materials and Methods

2.1. Synthesis and Characterization of C_{60}-Cu(NOTA)

All solvents and reagents were purchased from commercial sources and used as received. All synthetic reactions were performed under argon, unless otherwise stated. Matrix-assisted laser

desorption ionization mass spectrometry (MALDI-MS) was performed using an Autoflex MALDI ToF mass spectrometer (Bruker Corporation, Billerica, MA, USA). ^{1}H nuclear magnetic resonance (NMR) was performed using a 400 MHz NMR spectrometer (Bruker Corporation, Billerica, MA, USA). Fourier Transform Infrared (FTIR) spectroscopy was performed using a Nicolet 6700 FTIR spectrometer with an attenuated total reflectance (ATR) attachment (Thermo Fisher Scientific, Waltham, MA, USA). Purification of most intermediates was performed using a 971-FP Flash Purification System (Agilent Technologies, Inc., Santa Clara, CA, USA). All MS, ^{1}H NMR, and IR spectra are included in the ESI. The hydrodynamic diameter and aggregate diameter of the C_{60}-NOTA conjugate were determined by dynamic light scattering (DLS) and atomic force microscopy (AFM), respectively. The zeta-potential (ξ-potential) of the C_{60}-NOTA and C_{60}-Cu(NOTA) conjugates were determined as well. The DLS and ξ-potential measurements were conducted using a Zetasizer Nano system (Malvern Instruments, Malvern, UK). AFM images were taken using a MultiMode AFM-2 instrument (Digital Instruments, Santa Barbara, CA, USA).

High performance liquid chromatography (HPLC) was performed using 0.1% trifluoroacetic acid (TFA) in water (solvent A) and 0.1% TFA in acetonitrile (solvent B). Purification was performed on a 1260 Infinity II preparative HPLC (Agilent Technologies, Inc., Santa Clara, CA, USA) with the following method: 5% solvent B (in solvent A) to 30% solvent B over 15 min, then 30% solvent B to 95% solvent B over the next 15 min with a 15 mL/min flow rate. A Luna® C18 5 μm column with 21.2 × 250 mm dimensions (Phenomenex, Torrance, CA, USA) was used. Analytical HPLC was performed on an Agilent 1100 Series instrument using 5% solvent B to 95% solvent B over 15 min with a 1 mL/min flow rate. An XBridge® C18 3.5 μm column with 4.6 × 250 mm dimensions (Waters Corp., Milford, MA, USA) was used.

Synthesis of Compound **1**: Benzyl *N*-[(4-aminophenyl) methyl]carbamate (2.00 g, 7.80 mmol), ethyl hydrogen malonate (1.03 g, 7.80 mmol), and N, N-diisopropylethylamine (Hünig's base; 1.50 mL, 8.58 mmol) were dissolved in dry dichloromethane under argon at 0 °C. Diisopropylcarbodiimide (DIC; 1.25 mL, 7.96 mmol) was added dropwise over 10 min. The reaction was stirred and allowed to reach room temperature over 24 h. The solution was then dried by rotary evaporation that yielded an orange oil. Toluene was added to the oil until a white precipitate formed that was removed by vacuum filtration and discarded. The filtrate was purified by column chromatography using a gradient of dichloromethane/methanol as the eluent. The second fraction was then recrystallized from dichloromethane using hexanes, forming compound **1** as white needle-like crystals (0.376 g, 13% yield). m.p.: 108−109 °C. IR ν_{max} (neat): 3331, 3300, 2976, 1736, 1686, 1653, 1530, 1265, 1243, 1133, 1034, 971 cm^{-1}. ^{1}H NMR (400 MHz, CDCl$_3$): δ 9.23 (s, 1H), 7.48−7.44 (m, 2H), 7.35−7.27 (m, 5H), 7.22−7.17 (m, 2H), 5.34 (t, *J* = 5.9 Hz, 1H), 5.11 (s, 2H), 4.30 (d, *J* = 5.9 Hz, 2H), 4.22 (q, *J* = 7.2 Hz, 2H), 3.42 (*s*, 2H), 1.30 (t, *J* = 7.2 Hz, 3H). MALDI-MS: *m/z* calculated for $C_{20}H_{22}N_2O_5$, 370.398; found, 371.128 [M$^+$], 393.145 [M + Na$^+$], 409.203 [M + K$^+$].

Synthesis of Compound **2**: C_{60} (1.00 g, 1.39 mmol) was dissolved in 800 mL of dry toluene by bath sonication. Compound **1** (0.645 g, 1.74 mmol) and carbon tetrabromide (0.922 g, 2.78 mmol) were also added to the reaction mixture. A 1 M solution of 1,8-diazabicycloundec-7-ene (DBU) in toluene (1.94 mL, 1.94 mmol) was then added in two aliquots 10 min apart, and the reaction was stirred for 4.5 h at room temperature. A black precipitate formed during the reaction that was removed by vacuum filtration and discarded before the reaction mixture was purified by column chromatography using a gradient of toluene/ethyl acetate as the eluent. The second fraction was collected, and the solvent was removed by rotary evaporation to afford compound **2** as a dark red solid (0.121 mg, 8% yield). MALDI-MS: *m/z* calculated for $C_{80}H_{20}N_2O_5$, 1089.024; found, 1089.633 [M$^+$], 1112.690 [M + Na$^+$], 1127.620 [M + K$^+$].

Synthesis of Compound **3**: Compound **2** (0.048 g, 44.5 μmol) was dissolved in a 1:1 mixture of dry toluene and dry dichloromethane. *N*,*N'*-bis[2-(acetyloxy)-1-[acetyloxy)methyl]ethyl]-malonamide (protected serinolamide malonate; 0.187 g, 0.448 mmol), which was previously synthesized according to the method reported by Wharton et al. [33], was dissolved in dry dichloromethane and added

to the reaction flask. Carbon tetrabromide (0.221 g, 0.667 mmol) was then added to the reaction mixture followed by DBU (0.245 mL, 0.245 mmol) in 6 mL of toluene dropwise over 6 h. The reaction mixture was purified by column chromatography using a gradient of chloroform/methanol as the eluent. The first fraction was collected, and the solvent was removed by rotary evaporation giving compound **3** as a light red solid (0.128 g, 91% yield). IR ν_{max} (neat): 3294, 3064, 2958, 1736, 1663, 1538, 1366, 1219, 1041 cm^{-1}. MALDI-MS: *m/z* calculated for $C_{165}H_{140}N_{12}O_{55}$, 3170.919; found, 3169.637 [M$^+$], 3192.630 [M + Na$^+$].

Synthesis of Compound **4**: Trifluoroacetic acid (TFA; 3.10 µL, 40.5 µmol) was dissolved in isopropyl alcohol to give a 1.04 M solution. Compound **3** (0.128 g, 40.5 µmol) was then added along with methanol until everything was dissolved. Pd/C (0.27 g) was added to the reaction mixture, and the vial was placed in a pressurized vessel with 10.2 atm of H$_2$. The reaction mixture was stirred at room temperature for about 12 h. The mixture was then filtered by vacuum filtration to remove the Pd/C, and the solvent was removed by rotary evaporation to give compound **4** as a red solid without further purification (0.091 g, 74% yield). MALDI-MS: *m/z* calculated for $C_{157}H_{134}N_{12}O_{53}$, 3036.787; found, 3037.912 [M$^+$], 3058.515 [M + Na$^+$].

Synthesis of Compound **5**: Compound **4** (0.091 g, 29.9 µmol), 4-(4,7-bis(2-(*tert*-butoxy)-2-oxoethyl)-1,4,7-triazonan-1-yl)-5-(tert-butoxy)-5-oxopentanoic acid (NODAGA-t-Bu; 0.016 g, 29.9 µmol), and Hünig's base (5.73 µL, 32.9 µmol) were dissolved in dry dichloromethane at 0 °C. DIC (4.78 µL, 30.5 µmol) was then added dropwise over 10 min. The reaction was stirred for 12 h and warmed to room temperature as the reaction proceeded. The solvent was removed by rotary evaporation to afford compound **5** as a red solid without further purification. (0.093 g, 87% yield). IR ν_{max} (neat): 3323, 2979, 1739, 1680, 1538, 1368, 1224, 1150, 1046 cm^{-1}. MALDI-MS: *m/z* calculated for $C_{184}H_{181}N_{15}O_{60}$, 3562.463; found, 3564.097 [M$^+$].

Synthesis of Compound **6** *(C$_{60}$-NOTA conjugate)*: Compound **5** (0.091 g, 25.5 µmol) was dissolved in 10 mL of p-dioxane. 12 M HCl (0.833 mL) was added to the solution, and it was stirred for 5 d at room temperature under atmospheric conditions. The reaction mixture separated into two phases for the first 24 h. Distilled water was added at 48 h until the reaction mixture became homogeneous. After the fifth day, the mixture was dried using rotary evaporation, and the product was dissolved in distilled water and purified using dialysis centrifuge tubes with a 3500 molecular weight cut-off membrane in water that were stirred at 3600 rpm for 60 min. The dialysate was collected and subjected to additional dialysis using a 2000 molecular weight cut-off membrane cartridge in distilled water for two weeks. After drying by lyophilization, compound **6** was afforded as an orange solid (7.16 mg, 11% yield). The identity and purity of the compound was confirmed by analytical HPLC (retention time = 7.6 min) and ^{1}H NMR through confirmation that the acetate protecting groups on the serinolamide moieties had been completely hydrolyzed (absence of peak at 2.08 ppm). IR ν_{max} (neat): 3268, 3063, 2943, 2880, 1652, 1531, 1460, 1283, 1040 cm^{-1}. The C$_{60}$-NOTA conjugate was then dissolved in distilled water (<1 mg/mL) and analyzed using dynamic light scattering (DLS) to determine the hydrodynamic diameter. The C$_{60}$-NOTA solution was added to a disposable cuvette with a 1 cm path length and allowed to equilibrate for two minutes prior to sizing measurements. The obtained intensity profiles were used, and a correlation function was used to determine the intensity-weighted hydrodynamic diameter of samples. All measurements for a particular sample were combined to provide a statistical average at all sizes measured and plotted as an intensity profile. The ξ-potential of the C$_{60}$-NOTA conjugate was measured using disposable capillary cells using the same solution used to measure the hydrodynamic diameter. AFM images were obtained by making a dilute solution of the C$_{60}$-NOTA conjugate in isopropanol and drop-casting 2–4 drops of solution onto a mica substrate. The samples were analyzed in tapping mode with 512 lines at 0.5 Hz.

Synthesis of C$_{60}$-Cu(NOTA): CuCl$_2$ (1.30 mg, 10.0 µmol) was dissolved in 1 mL of 0.1 M NaOAc buffer, pH = 6. C$_{60}$-NOTA (6.40 mg, 2.50 µmol) was added in one portion under atmospheric conditions. The reaction mixture was heated to 45 °C, stirred overnight, and then purified using preparative HPLC

to afford the title compound as an orange solid. The ξ-potential of the C_{60}-Cu(NOTA) conjugate was measured as described above.

2.2. Radiochemistry Studies

All solvents and reagents were purchased from commercial sources and used as received. Water was deionized using a Milli-Q integral water purification system (MilliporeSigma, Burlington, MA, USA). [^{64}Cu]CuCl$_2$ was produced from a 16 MeV proton/deuteron GE PETtrace 10 cyclotron (GE Healthcare, Chicago, IL, USA) using an EDS/PTS solid target station (Comecer S.p.A., Castel Bolognese, Italy) in the Cyclotron Radiochemistry Facility at the MD Anderson Cancer Center. Radioactivity was detected during HPLC using a Bioscan Model 106 detector interfaced with the analytical HPLC through an Agilent Interface 35900E (same analytical and preparative instruments, methods, and columns as described in previous sections).

Radiolabeling of C_{60}-[^{64}Cu]Cu(NOTA): Cyclotron-produced [^{64}Cu]CuCl$_2$ in 0.1 M HCl (2.69 mCi, 3 μL) was added to 100 μL of 0.1 M NaOAc buffer, pH = 5.6. C_{60}-NOTA (80 μg, 31 nmol) in 40 μL of water was added, and the reaction was heated to 37 °C for 60 min. Reaction completion was confirmed with analytical HPLC. The reaction mixture was loaded onto a PD-10 column (GE Healthcare, Chicago, IL, USA) and eluted with 5 mL of 1 × phosphate buffered saline (PBS) in 500 μL fractions. A decay-corrected radiochemical yield of 49 ± 5% (n = 4) was obtained. C_{60}-[^{64}Cu]Cu(NOTA) was obtained in 98% purity with a molar activity of 1.35–3.06 GBq/μmol.

Radiolabeling of [^{64}Cu]Cu(NOTA): Cyclotron-produced [^{64}Cu]CuCl$_2$ in 0.1 M HCl (1.027 mCi, 1 μL) was added to 100 μL of 0.1M NaOAc buffer, pH = 5.6. NOTA (40 μg, 130 nmol) in 40 μL of water was added, and the reaction was heated to 37 °C for 45 min. Reaction completion was confirmed with analytical HPLC. The reaction mixture was buffered with 300 μL of 1X PBS and injected into mice without further purification. [^{64}Cu]Cu(NOTA) was obtained in >99% purity with a molar activity of 0.268–0.601 GBq/μmol.

Shelf and Serum Stability Studies: C_{60}-[^{64}Cu]Cu(NOTA) (120 μCi, 200 μL) was incubated with 200 μL of human serum at 37 °C. After 20 and 48 h, the sample was analyzed with analytical HPLC to determine integrity. A shelf stability test with C_{60}-[^{64}Cu]Cu(NOTA) (529 μCi, 500 μL) and [^{64}Cu]Cu(NOTA) (235 μCi, 90 μL) in PBS was also conducted at room temperature and at 4 °C. After 24 and 48 h, the samples were analyzed with analytical HPLC to determine integrity.

2.3. PET Imaging and Metabolism Studies

PET and CT scans were performed using a small animal Albira PET/SPECT/CT scanner (Bruker Corporation, Billerica, MA, USA). PET images were analyzed using PMOD Version 3.505 (PMOD Technologies Ltd., Zürich, Switzerland). PET/CT maximum intensity projections were constructed using Inveon Research Workplace (Siemens Medical Solutions USA, Inc., Malvern, PA, USA). Statistical analysis was performed on GraphPad Prism 8 (GraphPad Software, San Diego, CA, USA).

PET Image Acquisition: All mice were manipulated in accordance to the MD Anderson Cancer Center's IACUC guidelines. Mice were anesthetized with 2% isoflurane using oxygen as a carrier. For both C_{60}-[^{64}Cu]Cu(NOTA) and [^{64}Cu]Cu(NOTA), 6 male nude mice were injected on the bed with ~200 μCi of activity in 150 μL of saline through a tail vein catheter. At the start of injection, a 20-min dynamic PET scan was acquired using the Albira PET/SPECT/CT scanner with a 15 cm field of view (FOV). The actual injected dose was calculated by measuring the pre- and post-injection activity in the syringe using a CRC-15R dose calibrator (Capintec, Inc., Florham Park, NJ, USA). The data were binned into 20-s time frames for the first 5 min, 60-s frames for the next 5 min, and 5-min frames for the next 10 min. Static PET images were then recorded at 3 h and 24 h post-injection (p.i.) for 10 min. A static PET image at 48 h p.i. was recorded for 20 min for C_{60}-[^{64}Cu]Cu(NOTA) only. Following all PET scans, two 3 min CT scans were performed to cover the whole mouse body with a total FOV of 12.6 cm (400 μA, 45 kV, 250 projections).

The PET images were reconstructed using the Maximum Likelihood Expectation Maximization method with 12 iterations. The CT images were reconstructed using the Filtered Back Projection method. Scatter, randoms, decay, and attenuation corrections were applied through the Albira software. Volumes-of-interest (VOIs) were drawn for the major organs on the decay-corrected PET images using PMOD, and injected doses were used to calculate percent of injected dose per cubic centimeter of tissue (%ID/cc). Errors in the averaged %ID/cc were reported as standard error of the mean (SEM). A non-linear regression analysis of the dynamic PET data for both C_{60}-[^{64}Cu]Cu(NOTA) and [^{64}Cu]Cu(NOTA) was performed and fitted to a two-phase decay model to determine the blood half-life of each compound.

Metabolism Stability Studies: 179 µCi, 204 µCi, and 205 µCi of C_{60}-[^{64}Cu]Cu(NOTA) were injected through a tail vein catheter into three nude mice under anesthesia with 2% isoflurane using oxygen as a carrier. The mice remained anesthetized, and blood and urine were collected from each mouse after 20 min and rapidly cooled on dry ice to halt metabolism. The urine was injected directly onto the analytical HPLC. The blood was centrifuged with acetonitrile, and the serum/acetonitrile layer was injected onto the analytical HPLC. Additional urine was collected from anesthetized mice at 24 h and injected directly onto the analytical HPLC.

3. Results

3.1. Synthesis and Characterization of C_{60}-NOTA Conjugate

The structure of a C_{60}-serinol derivative amenable to PET imaging was constructed to include a chelate that could be radiolabeled with copper-64. The bifunctional chelate derivative of NOTA (2-(4,7-bis(carboxymethyl)-1,4,7-triazonan-1-ylpentanedioic acid, or NODAGA) was chosen as NOTA has been shown to exhibit high kinetic stability for copper in radiochemical studies when compared to other chelates [44–46]. The C_{60}-NOTA conjugate was synthesized according to the procedure outlined in Experimental Section 2.1 (Figure 2). Compound **1** was formed using a DIC-mediated amide bond formation reaction between benzyl *N*-[(4-aminophenyl)methyl]carbamate and ethyl hydrogen malonate in the presence of Hünig's base. Formation of compound **2** utilized a Bingel-Hirsch reaction with the derivatized malonate to replace one 6–6 double bond of fullerene with a cyclopropane ring after in situ formation of the bromomalonate. The monoadduct was easily separated from unreacted C_{60} and the bisadduct using column chromatography. A subsequent Bingel-Hirsch reaction was then performed with a large excess of the protected serinolamide compared to compound **2** to control the number of groups added to the surface. Slow DBU addition and long reaction times also led to the formation of higher adduct products. The hexakisadduct (compound **3**) showed a favorable formation using these conditions; however, a small amount of pentakisadduct occasionally remained in the final product. The benzyloxy carbamate protecting group was then removed from the malonate linker via hydrogenolysis, and the tert-butyl protected NOTA chelate was added through another DIC-mediated coupling in the presence of Hünig's base to give compound **5**. Finally, a global acid deprotection removed the tert-butyl and acetate protecting groups to give the final C_{60}-NOTA conjugate (compound **6**).

The C_{60}-NOTA material (compound **6**) was characterized by FTIR spectroscopy to confirm introduction of functional groups to the C_{60} cage. The FTIR spectrum of C_{60}-NOTA was distinct from that of the naked C_{60} and the serinolamide groups (Figure 3A). C_{60}-NOTA contained peaks at 1410, 1652, 2943, and 3268 cm^{-1} representing the carboxylic acid O-H stretch from NOTA, the C=C stretch of the C_{60} cage, the N-H stretch from serinolamide and NOTA linker malonates, and the O-H stretch from the many hydroxyls on the serinolamide groups, respectively. Dynamic light scattering (DLS) was employed to measure the hydrodynamic diameter of the nanostructure in solution (Figure 3B). The DLS measurements showed that C_{60}-NOTA conjugate forms uniform aggregates in water with an average diameter of 182 nm and an average polydispersity index of 0.27. These results agreed with the aggregate size that C_{60}-serinol itself has shown to form in aqueous solution (median aggregate size

100–200 nm) [47]. These DLS results were also in good agreement with the aggregate size found in the solid state as determined by atomic force microscopy (AFM) images (Figure S11) which showed the average aggregate size to be 195 nm.
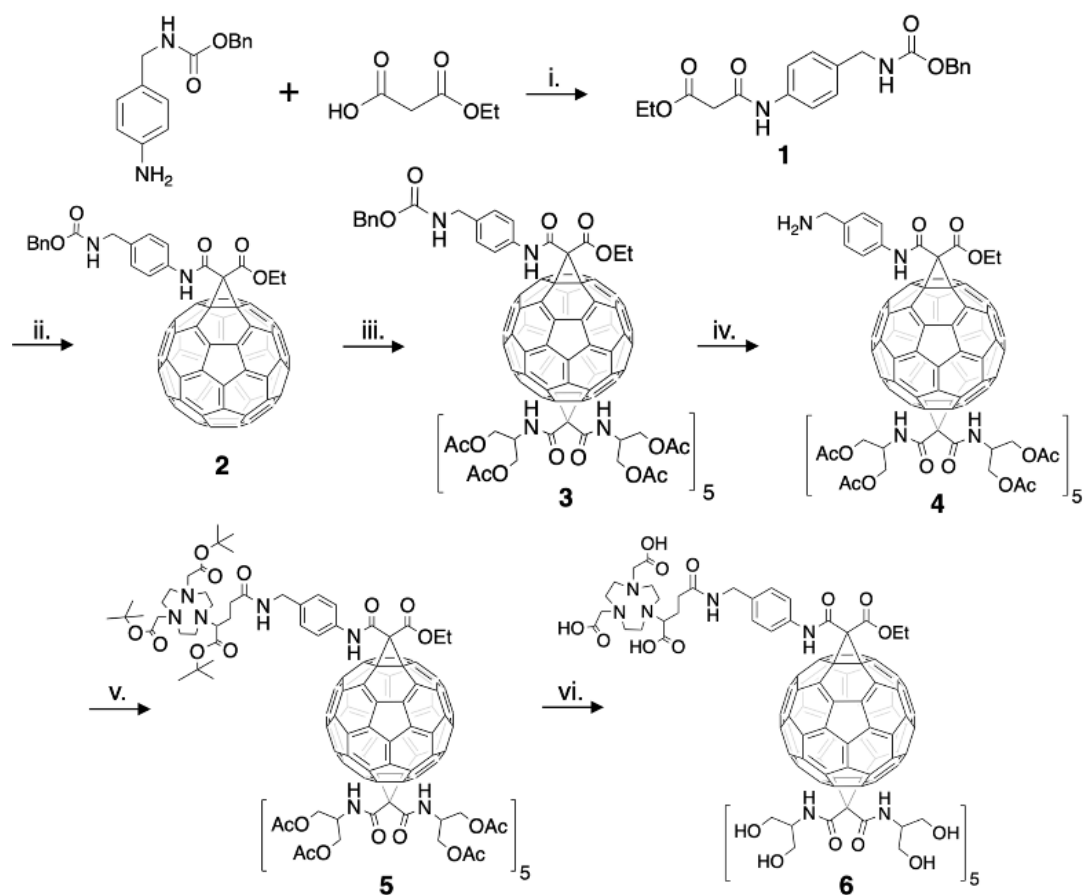

Figure 2. Complete synthesis of the C_{60}-NOTA conjugate (compound **6**). **i**: DIC, Hünig's base, 0 °C → RT, 12 h, 13% yield. **ii**: C_{60}, CBr$_4$, DBU, RT, 4.5 h, 8% yield. **iii**: *N,N'*-bis[2-(acetyloxy)-1-[acetyloxy)methyl]ethyl]-malonamide, CBr$_4$, DBU, RT, 6 h, 91% yield. **iv**: H$_2$, Pd/C, RT, 12 h, 74% yield. **v**: NODAGA-t-Bu, DIC, Hünig's base, 0 °C → RT, 12 h, 87% yield. **vi**: 1 N HCl, dioxane, RT, 4-5 d, 11% yield.

The C_{60}-NOTA conjugate was then chelated with nonradioactive Cu^{2+} to demonstrate the chelating ability of NOTA while appended to the C_{60} cage. Following a literature procedure [48], the material was labeled with CuCl$_2$ dissolved in an sodium acetate buffer at pH 6, which was then stirred overnight at 45 °C. The metallated conjugate, C_{60}-Cu(NOTA), the unmetallated conjugate, C_{60}-NOTA, and the unmetallated chelate, NOTA, were characterized by HPLC and were found to have different retention times (2.8 min for NOTA, 7.0 min for C_{60}-Cu(NOTA) and 7.6 min for C_{60}-NOTA; Figure 3C). These results demonstrated that conjugation of NOTA to C_{60} was successful and that the chelate successfully bound copper. Furthermore, the HPLC plots show there is no free NOTA within the C_{60}-NOTA material, which would have been problematic during the radiolabeling because NOTA and C_{60}-NOTA would compete for chelation with copper-64. The ζ-potential of C_{60}-NOTA and C_{60}-Cu(NOTA) were also investigated to determine the surface charge on the conjugate, which can affect the biodistribution of the material [49]. The ζ-potential of C_{60}-NOTA and C_{60}-Cu(NOTA) were −22.5 mV and −11.4 mV, respectively, which agrees well with ζ-potential measurements of C_{60}-serinol and other water soluble C_{60} materials [39,47,50].
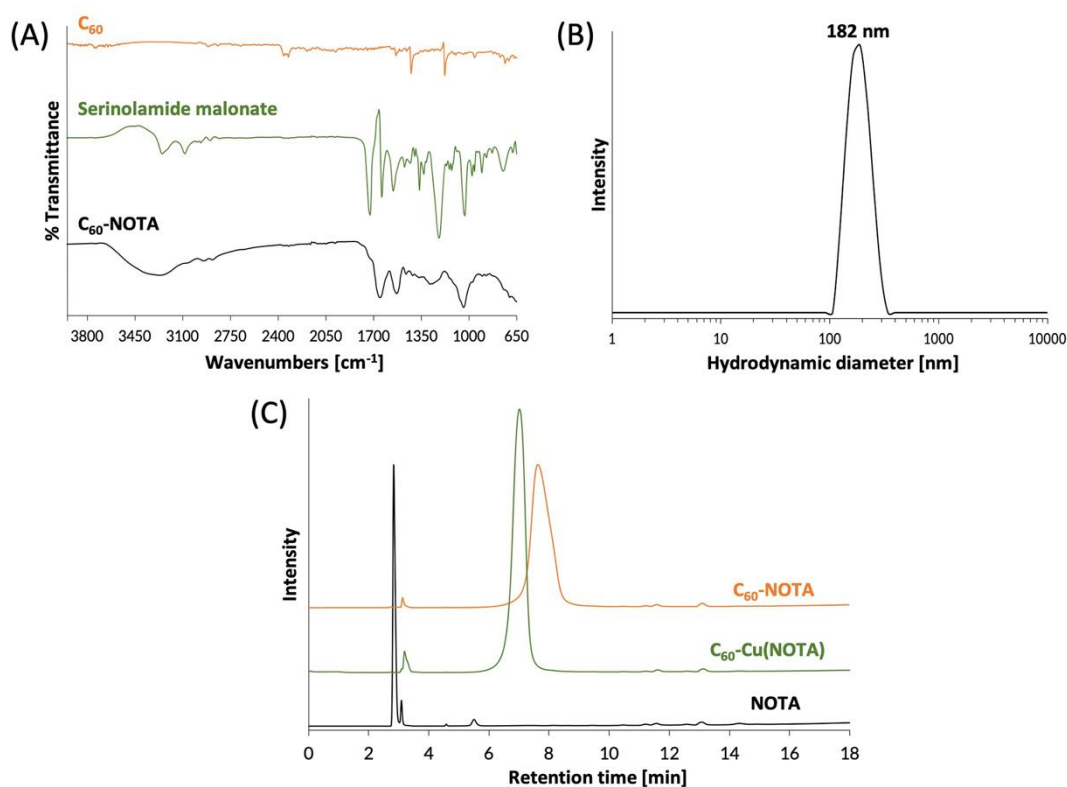
Figure 3. Chemical characterization of C_{60}-NOTA. (**A**) FTIR spectra of naked C_{60} (orange), the deprotected serinolamide malonate compound that is conjugated to the C_{60} cage (green), and the C_{60}-NOTA conjugate (black); (**B**) DLS spectrum showing the hydrodynamic diameter of C_{60}-NOTA; (**C**) HPLC chromatograms of C_{60}-NOTA (orange), C_{60}-Cu(NOTA) (green), and NOTA alone (black). Peak at 3.1 min is an impurity in the commercial NOTA compound that did not affect radiochemistry.

3.2. Radiolabeling of C_{60}-NOTA

The C_{60}-NOTA conjugate was radiolabeled with copper-64, and its radiochemical purity and stability in biological media were evaluated. The conjugate was radiolabeled with copper-64 in a sodium acetate buffer (pH 5.6) at 37 °C for 1 h and tracked by analytical radio-HPLC (Figure 4). C_{60}-[^{64}Cu]Cu(NOTA) exhibited a different retention time than [^{64}Cu]Cu(NOTA) and free copper-64 on radio-HPLC. After purification, a decay-corrected yield of 49 ± 5% (n = 4) was obtained, and the radio-HPLC chromatograms show that C_{60}-[^{64}Cu]Cu(NOTA) had a radiochemical purity of 97%. Furthermore, the metal ion stability of C_{60}-[^{64}Cu]Cu(NOTA) was challenged in PBS for 24 and 48 h at 25 °C and human serum for 20 and 48 h at 37 °C (Figures S13 and S14). C_{60}-[^{64}Cu]Cu(NOTA) proved to be 93% and 95% stable in PBS at 24 h and 48 h, respectively. In addition, C_{60}-[^{64}Cu]Cu(NOTA) was 91% and 89% stable in human serum at 20 h and 48 h, respectively.
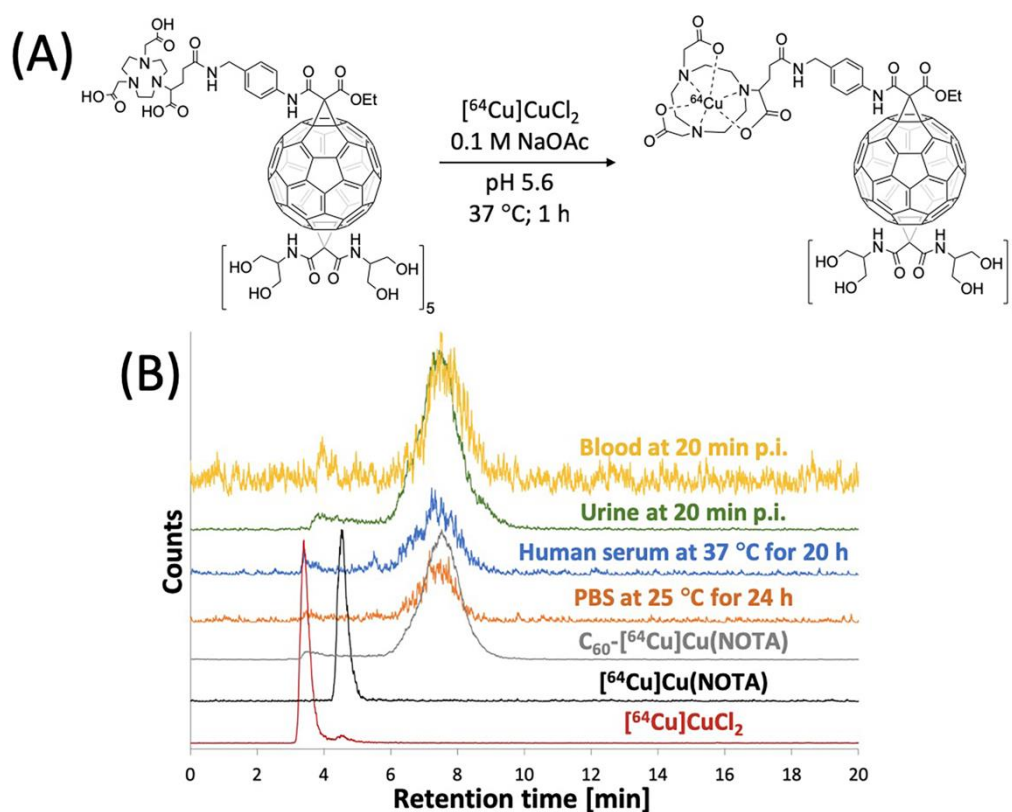
Figure 4. Radiolabeling of C_{60}-NOTA. (**A**) Radiolabeling reaction scheme; (**B**) Radio-HPLC chromatograms of $[^{64}Cu]CuCl_2$ (red), $[^{64}Cu]Cu(NOTA)$ (black), and C_{60}-$[^{64}Cu]Cu(NOTA)$ (gray), C_{60}-$[^{64}Cu]Cu(NOTA)$ challenged against PBS at 25 °C for 24 h (orange), C_{60}-$[^{64}Cu]Cu(NOTA)$ challenged against human serum at 37 °C for 20 h (blue), mouse urine sample at 20 min p.i. (green), and mouse blood sample at 20 min p.i. (yellow).

3.3. PET Imaging of C_{60}-$[^{64}Cu]Cu(NOTA)$

C_{60}-$[^{64}Cu]Cu(NOTA)$ was then administered to mice by tail-vein injection of ~200 µCi in 150 µL of saline, and mice were imaged by PET/CT. First, a 20-min dynamic scan was acquired for each animal, followed by static scans that were taken at 3, 24, and 48 h p.i. (Figure 5). Representative PET images (Figure 5A) and the time activity curve (TAC) of the dynamic scan (Figure 5B) show that C_{60}-$[^{64}Cu]Cu(NOTA)$ accumulated in tissues as it circulated and then decreased rapidly in all organs except the kidneys. The conjugate material cleared rapidly from the heart, liver, and lungs over the first 6 min, while showing negligible uptake in the brain and muscle. At 20 min p.i., the kidneys and bladder still had the highest uptake of C_{60}-$[^{64}Cu]Cu(NOTA)$, as seen in the PET image for that time point. The amount of radioactivity significantly decreased at 3 and 24 h p.i. for all organs, and there was negligible uptake for any organ at 48 h, indicating the material had effectively cleared from the mice (Figure 5C). These biodistribution data resemble trends seen for X-ray contrast agents functionalized with serinolamide groups including the rapid renal clearance [32].

Because PET detects signal from the radioactive copper-64 ion and not from the fullerene compound itself, it was important to assess C_{60}-$[^{64}Cu]Cu(NOTA)$ stability in vivo. To answer this question, blood and urine samples from mice were collected at 20 min p.i. and analyzed using radio-HPLC to determine the integrity of the excreted material (Figure 4B). These data indicated that the conjugate is highly stable in vivo with 97% and 92% retention of copper in urine and blood, respectively. Furthermore, there was no evidence that any $[^{64}Cu]Cu(NOTA)$ was cleaved from the fullerene conjugate, which suggested the material was excreted without significant modification.
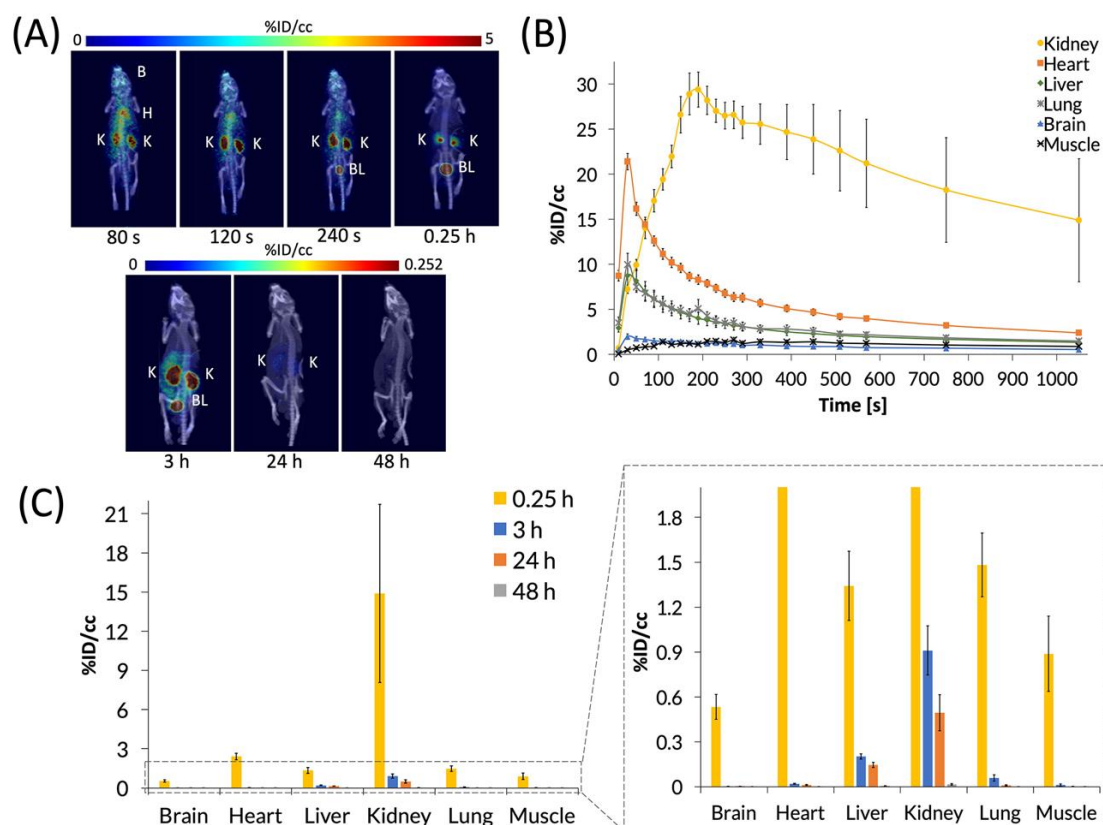
Figure 5. PET images and biodistribution of C_{60}-[^{64}Cu]Cu(NOTA). (**A**) Whole-body dynamic and static PET images acquired at various time points post-injection (p.i.). Organs labeled are brain (B), heart (H), kidney (K), and bladder (BL); (**B**) Time activity curve (TAC) of 20 min dynamic scan showing initial biodistribution and rapid decrease in uptake in most organs; (**C**) Quantification of radioactivity in VOIs showing accumulation in various organs with a close-up view of the graph to highlight lower accumulation. Data represent mean ± SEM, n = 6.

3.4. PET Imaging of [^{64}Cu]Cu(NOTA)

After characterizing the biodistribution of the C_{60}-[^{64}Cu]Cu(NOTA) conjugate, we sought to examine how the biodistribution of [^{64}Cu]Cu(NOTA) compares to that of the C_{60} conjugate (Figure 6). These studies showed that [^{64}Cu]Cu(NOTA) has a similar biodistribution profile to C_{60}-[^{64}Cu]Cu(NOTA) with significant uptake in the kidneys at 20 min p.i. compared to other major organs at the same time point. However, accumulation decreased rapidly at 3 and 24 h p.i. Although mice were imaged at 48 h p.i., the detected signal was negligible. This evidence indicated that most of the material was cleared by renal excretion between 20 min and 3 h p.i. These data are supported by previous biodistribution studies of other small-molecule, macrocyclic copper chelates of similar structure, such as DOTA and TETA, which were also found to be almost completely cleared within 24 h [51].

We also performed a non-linear regression analysis of the heart TAC data of both compounds using a two-phase decay model, which produced a *p* value of < 0.0001 by an extra sum-of-squares F test. The two-phase decay model consists of a distribution phase and an elimination phase. The fast distribution phase describes the rapid circulation of the material from the plasma to highly-perfused tissues, and the slow elimination phase describes the clearance of the material from the plasma and tissues through excretion. From this analysis, a blood half-life ($t_{1/2}$) and rate constants (α, β) for each phase were determined along with the clearance rate (CL) and the area under the curve (AUC), which represents a normalized volume of distribution (Table 1).
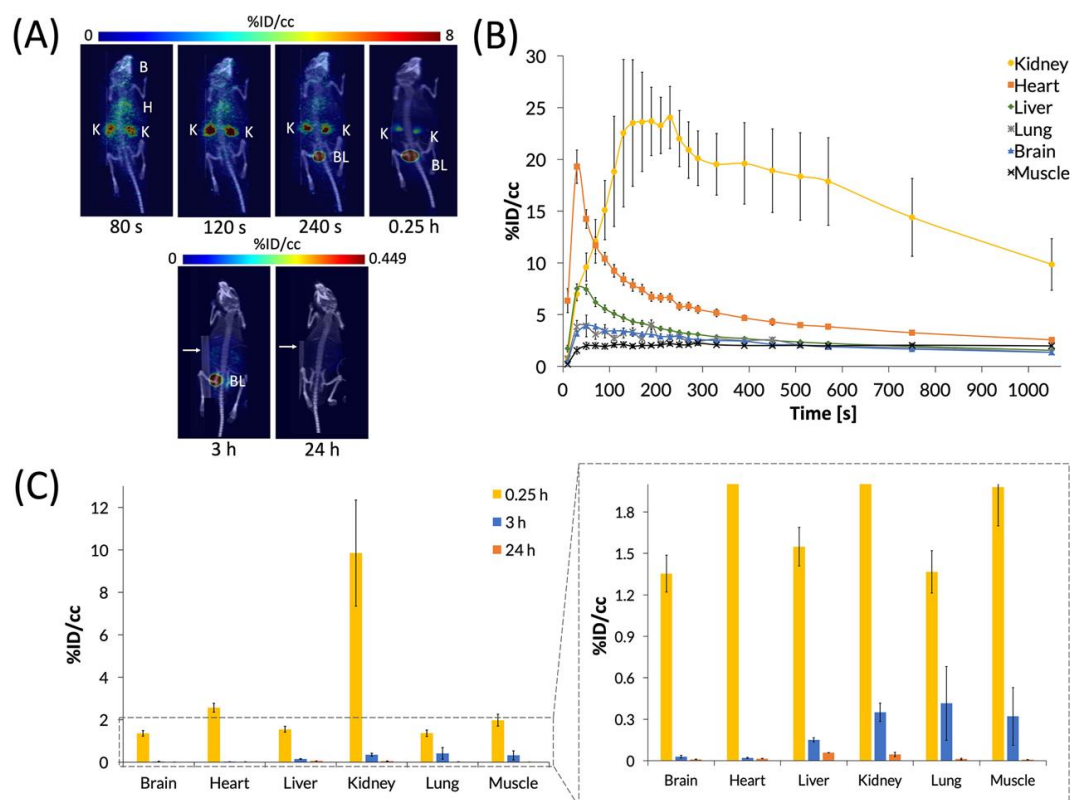
Figure 6. PET images and biodistribution of [^{64}Cu]Cu(NOTA). (**A**) Whole-body dynamic and static PET images acquired at various time points post-injection (p.i.). Organs labeled are brain (B), heart (H), kidney (K), and bladder (BL). White arrows for 3 and 24 h p.i. images highlight a breathing pad that was placed under the mice during imaging. The radioactivity was negligible at 48 h p.i., so it could not be imaged and quantified accurately, suggesting that [^{64}Cu]Cu(NOTA) was no longer present in vivo at 48 h p.i.; (**B**) The time activity curve (TAC) of a 20 min dynamic scan showing initial biodistribution and rapid drop-off in uptake in most organs; (**C**) Quantification of radioactivity in various organs with a vertically expanded view of the graph to highlight lower accumulation. Data represent mean ± SEM, n = 6.

Table 1. Pharmacokinetic Parameters for C$_{60}$-[^{64}Cu]Cu(NOTA) and [^{64}Cu]Cu(NOTA) [1].

Material	Distribution Half-Life [min]	Distribution Rate Constant (α) [min^{-1}]	Elimination Half-Life [min]	Elimination Rate Constant (β) [min^{-1}]	Clearance (CL) [cc/min]	Area under Curve (AUC) [%ID·min/cc]
C$_{60}$-[^{64}Cu]Cu(NOTA)	0.6436	1.077	7.078	9.793×10^{-2}	3.161×10^{-5}	3.164×10^{2}
[^{64}Cu]Cu(NOTA)	0.4975	1.393	8.153	8.501×10^{-2}	3.152×10^{-5}	3.173×10^{2}

[1] Two-phase decay model: R^2 = 0.966 for C$_{60}$-[^{64}Cu]Cu(NOTA) and for [^{64}Cu]Cu(NOTA).

4. Discussion

C$_{60}$-[^{64}Cu]Cu(NOTA) was produced in high yields and radiochemical purity, was found to retain copper-64 higher than 90% in in vitro and in vivo studies, and was administered intravenously in mice to assess its biodistribution by PET/CT. A dynamic 20 min PET scan was acquired, followed by static 3, 24 and 48 h post injection follow-up scans. The radiolabeled fullerene cleared very quickly through the kidneys in the first hour post injection, with very minimal accumulation in the other organs at later time points. This was somewhat surprising as nanoparticles tend to have a hepatobiliary clearance pathway. Our group and others have shown that carbon nanotubes and other types of nanoparticles typically localize to the lungs, liver, and spleen [1,3,5,52–54]. Mechanistically, as previously described by Aggarwal, et al. protein aggregation around nanoparticles increases with the more hydrophobic

surface exposed, leading to macrophage uptake and excretion through reticuloendothelial system (RES) organs [55]. In our work, it is likely that coating the hydrophobic surface of C_{60} with hydrophilic serinolamide groups prevented such aggregation and allowed for C_{60}-[^{64}Cu]Cu(NOTA) to be excreted through the kidneys as single particles. In addition, C_{60}-[^{64}Cu]Cu(NOTA) did not significantly collect in the lungs or liver, which also mitigates long-term toxicity concerns of fullerenes [56].

As is the case with any nanomaterial, surface chemistry is known to play an important role in the material's in vivo behavior [57]. For example, there have been many reports of C_{60} derivatives with less hydrophilic coverage than that of the present study, such as hydroxylated and carboxylated fullerenes, which showed greater retention in the lungs, muscle, and RES organs, in addition to longer residence times in vivo (~30 h) [26,38,41,58–61]. However, leaving some lipophilic character on the C_{60} surface can result in the penetration of certain restrictive membranes, such as the blood-brain-barrier, as was recently reported by Dugan and coworkers when administering ^{14}C-labeled e,e,e-methanofullerene(60)-63-tris malonic acid (C_3) [40]. C_3 showed significant liver and kidney uptake at 12 and 24 h p.i., which resulted in fecal excretion as the route of clearance. These examples contrast with the C_{60}-[^{64}Cu]Cu(NOTA) conjugate of this work, which only showed rapid renal clearance under 3 h.

While the above examples showed studies that observed long in vivo residence times for fullerene derivatives, one study reported a fast-clearing amino-PEGylated C_{60} derivative [39]. The authors analyzed this material that had a similar diameter and surface charge as our construct, which was also radiolabeled with [^{64}Cu]Cu(NOTA). While the biodistribution data reported by these authors at later time points generally agree with the results presented here, conducting a dynamic PET scan after administration of C_{60}-[^{64}Cu]Cu(NOTA) allowed us to study the biodistribution profile more thoroughly, which was especially important when evaluating a material that clears this quickly. Overall, these similar results to our work show that masking the hydrophobic surface of C_{60} with different hydrophilic groups can effectively lead to fast renal clearance. Furthermore, this group examined the toxicity of their material and found that the compound was not cytotoxic at 100 µg/mL exposure [39]. We have previously shown that C_{60}-serinol is likewise non-cytotoxic at the same concentration [34].

From the blood half-life data (Table 1), it is evident that clearance characteristics are similar for C_{60}-[^{64}Cu]Cu(NOTA) and the [^{64}Cu]Cu(NOTA) control agent. While the appended imaging agent has potential to influence the pharmacokinetics of C_{60}-[^{64}Cu]Cu(NOTA), both C_{60}-[^{64}Cu]Cu(NOTA) and [^{64}Cu]Cu(NOTA) had similar "small molecule-like" behavior in vivo. C_{60}-[^{64}Cu]Cu(NOTA) clears more quickly from the blood, with distribution and elimination half-life values of 0.6436 and 7.078 min respectively, compared to reported C_{60}-drug conjugates with similar hydrodynamic diameters and ξ-potentials with elimination half-life values between 200–500 min [62,63]. These C_{60}-drug conjugates bound to monomethyl fumarate and tamoxifen were both made water soluble with four units of PEG (tetraethylene glycol). Another study reported an even longer $t_{1/2}$ (1.8×10^4 min), which is likely due to the hydrophobic nature of the conjugate, as it was derivatized with the hydrophobic drug docetaxel [64].

Comparing present results for C_{60}-[^{64}Cu]Cu(NOTA) to our previous work with a fluorescently-labeled C_{60}-serinol-PF conjugate (Figure 1) [34], we found dramatically different profiles even though both nanomaterials are derivatives of C_{60}-serinol. C_{60}-serinol-PF was observed as predominately retaining in the tumor, kidneys, liver, and brain in a liver cancer mouse model (Hep3B) for longer than 100 h p.i. Although no tumor model was used in the present study, the C_{60}-[^{64}Cu]Cu(NOTA) conjugate showed little uptake in the liver at 24 h p.i. and essentially no uptake in the brain. These strikingly different biodistribution profiles raise the question as to why these two C_{60}-serinol-based materials behave differently in vivo. Controls for the effects of derivatization of various nanomaterials are often lacking in the literature [61], and unfortunately, a control experiment examining the biodistribution of the PF fluorophore alone is not available. While the biodistribution pattern of C_{60}-[^{64}Cu]Cu(NOTA) nanomaterial is similar to that of the [^{64}Cu]Cu(NOTA) imaging tag, it is quite distinguished from that of the fluorescently-labeled C_{60}-serinol-PF. The biodistribution data for C_{60}-serinol-PF also showed significant uptake in the heart at greater than 100 h p.i., indicating

that the material was still circulating in the blood as a blood-pool agent. In fact, a recent study of C_{60}-serinol-PF biotransport kinetics reported that the material does not leak from normal vasculature as it does in tumor vasculature [47], leading to the conclusion that the PF fluorophore converts the C_{60}-serinol platform into a blood pool agent.

While the in vivo data presented here for C_{60}-[^{64}Cu]Cu(NOTA) provides evidence that C_{60}-serinol could serve as an ideal platform for designing a C_{60}-based biomedical material, further work should be done to tailor the biodistribution to the desired application. For example, there are 30 theoretical sites available on C_{60} for Bingel-Hirsch chemistry [65], and based on our experience, only two of those sites are required for serinolamide moieties to achieve water solubility. Therefore, reducing the hydrophilic character of C_{60}-serinol, as well as further functionalizing the surface with targeting agents to deliver therapeutic cargo is likely to increase residence time in vivo and make C_{60}-serinol better suited for drug delivery. It is also important to note that the biodistribution of any therapeutic cargo that C_{60}-serinol would carry can have a significant impact on the delivery of that cargo. Moreover, using a C_{60}-based drug delivery vehicle allows for the potential of multimodal therapy by also utilizing the attractive therapeutic properties of the C_{60} core, such as potent antioxidant activity and PDT capabilities [66], which is not possible with simply targeting small-molecule drugs or sequestering drugs within liposomes. While more work is necessary to tailor the delivery of drug cargo using C_{60}-serinol, it is clear through the in vivo data for the nanostructure that it is a benign platform with ideal in vivo behavior for biomedical applications including utilizing the inherent properties of C_{60} in concert with small-molecule drugs.

5. Conclusions

Herein, we have presented the synthesis, characterization, radiolabeling, and PET-determined biodistribution of a highly water-soluble C_{60} derivative, based on a C_{60}-serinol platform. It was demonstrated by comparing the biodistribution and pharmacokinetic parameters of C_{60}-[^{64}Cu]Cu(NOTA) and [^{64}Cu]Cu(NOTA) that C_{60}-[^{64}Cu]Cu(NOTA) exhibits "small molecule-like" behavior in vivo with quick renal clearance. This study provides rationale for conducting a control imaging study for the imaging agent when performing biodistribution studies on C_{60} derivatives. In addition, using radionuclides as an imaging tag for these biodistribution studies allows for tracking in vivo with high sensitivity and accuracy using non-invasive PET imaging over time. Therefore, the work presented here provides valuable insights about the rational design of future biomedical nanoparticles and demonstrates effective methods to evaluate the biodistribution and pharmacokinetics of these interesting materials.

References

1. Benezra, M.; Penate-Medina, O.; Zanzonico, P.B.; Schaer, D.; Ow, H.; Burns, A.; DeStanchina, E.; Longo, V.; Herz, E.; Iyer, S.; et al. Multimodal silica nanoparticles are effective cancer-targeted probes in a model of human melanoma. *J. Clin. Investig.* **2011**, *121*, 2768–2780. [CrossRef]

2. Reddy, L.H.; Arias, J.L.; Nicolas, J.; Couvreur, P. Magnetic Nanoparticles: Design and Characterization, Toxicity and Biocompatibility, Pharmaceutical and Biomedical Applications. *Chem. Rev.* **2012**, *112*, 5818–5878. [CrossRef]

3. Hernández-Rivera, M.; Zaibaq, N.G.; Wilson, L.J. Toward carbon nanotube-based imaging agents for the clinic. *Biomaterials* **2016**, *101*, 229–240. [CrossRef]

4. Zaibaq, N.G.; Moghaddam, S.E.; Wilson, L.J. Imaging and Treating Cancer with Carbon Nanotube Technology. In *Nanooncology*; Gonçalves, G., Tobias, G., Eds.; Springer International Publishing: Cham, Switzerland, 2018; pp. 173–210. ISBN 978-3-319-89877-3.

5. Biagiotti, G.; Pisaneschi, F.; Gammon, S.T.; Machetti, F.; Ligi, M.C.; Giambastiani, G.; Tuci, G.; Powell, E.; Piwnica-Worms, H.; Pranzini, E.; et al. Multiwalled carbon nanotubes for combination therapy: A biodistribution and efficacy pilot study. *J. Mater. Chem. B* **2019**, *7*, 2678–2687. [CrossRef] [PubMed]

6. Sanvicens, N.; Marco, M.P. Multifunctional nanoparticles—Properties and prospects for their use in human medicine. *Trends Biotechnol.* **2008**, *26*, 425–433. [CrossRef] [PubMed]

7. Cho, K.; Wang, X.; Nie, S.; Shin, D.M. Therapeutic Nanoparticles for Drug Delivery in Cancer. *Clin. Cancer Res.* **2008**, *14*, 1310–1316. [CrossRef] [PubMed]

8. Arruebo, M.; Vilaboa, N.; Sáez-Gutierrez, B.; Lambea, J.; Tres, A.; Valladares, M.; González-Fernández, Á. Assessment of the evolution of cancer treatment therapies. *Cancers (Basel)* **2011**, *3*, 3279–3330. [CrossRef] [PubMed]

9. Gao, X.J.; Shen, X.; Xing, G.; Gao, X. Fullerenes for Cancer Therapy and Bioimaging. In *Nanooncology: Engineering Nanomaterials for Cancer Therapy and Diagnosis*; Nanomedicine and Nanotoxicology; Gonçalves, G., Tobias, G., Eds.; Springer International Publishing: Cham, Switzerland, 2018; pp. 387–415. ISBN 978-3-319-89878-0.

10. Hirsch, A.; Grösser, T.; Skiebe, A.; Soi, A. Synthesis of Isomerically Pure Organodihydrofullerenes. *Chem. Ber.* **1993**, *126*, 1061–1067. [CrossRef]

11. Hirsch, A. Addition reactions of buckminsterfullerene (c60). *Synthesis* **1995**, *1995*, 895–913. [CrossRef]

12. Camps, X.; Hirsch, A. Efficient cyclopropanation of C60 starting from malonates. *J. Chem. Soc. Perkin Trans.* **1997**, *1*, 1595–1596. [CrossRef]

13. Yamago, S.; Tokuyama, H.; Nakamura, E.; Prato, M.; Wudl, F. Chemical derivatization of organofullerenes through oxidation, reduction, and carbon-oxygen and carbon-carbon bond-forming reactions. *J. Org. Chem.* **1993**, *58*, 4796–4798. [CrossRef]

14. Kampe, K.-D.; Egger, N.; Vogel, M. Diamino- und Tetraaminoderivate von Buckminsterfulleren C60. *Angew. Chem.* **1993**, *105*, 1203–1205. [CrossRef]

15. Semenov, K.N.; Charykov, N.A.; Postnov, V.N.; Sharoyko, V.V.; Vorotyntsev, I.V.; Galagudza, M.M.; Murin, I.V. Fullerenols: Physicochemical properties and applications. *Prog. Solid State Chem.* **2016**, *44*, 59–74. [CrossRef]

16. Semenov, K.N.; Charykov, N.A.; Keskinov, V.N. Fullerenol Synthesis and Identification. Properties of the Fullerenol Water Solutions. *J. Chem. Eng. Data* **2011**, *56*, 230–239. [CrossRef]

17. Dugan, L.L.; Lovett, E.G.; Quick, K.L.; Lotharius, J.; Lin, T.T.; O'Malley, K.L. Fullerene-based antioxidants and neurodegenerative disorders. *Park. Relat. Disord.* **2001**, *7*, 243–246. [CrossRef]

18. Ali, S.S.; Hardt, J.I.; Quick, K.L.; Sook Kim-Han, J.; Erlanger, B.F.; Huang, T.; Epstein, C.J.; Dugan, L.L. A biologically effective fullerene (C60) derivative with superoxide dismutase mimetic properties. *Free. Radic. Boil. Med.* **2004**, *37*, 1191–1202. [CrossRef]

19. Quick, K.L.; Ali, S.S.; Arch, R.; Xiong, C.; Wozniak, D.; Dugan, L.L. A carboxyfullerene SOD mimetic improves cognition and extends the lifespan of mice. *Neurobiol. Aging* **2008**, *29*, 117–128. [CrossRef]

20. Baati, T.; Bourasset, F.; Gharbi, N.; Njim, L.; Abderrabba, M.; Kerkeni, A.; Szwarc, H.; Moussa, F. The prolongation of the lifespan of rats by repeated oral administration of [60] fullerene. *Biomaterials* **2012**, *33*, 4936–4946. [CrossRef]

21. Mroz, P.; Xia, Y.; Asanuma, D.; Konopko, A.; Zhiyentayev, T.; Huang, Y.Y.; Sharma, S.K.; Dai, T.; Khan, U.J.; Wharton, T.; et al. Intraperitoneal photodynamic therapy mediated by a fullerene in a mouse model of abdominal dissemination of colon adenocarcinoma. *Nanomedicine* **2011**, *7*, 965–974. [CrossRef]

22. Serda, M.; Ware, M.J.; Newton, J.M.; Sachdeva, S.; Krzykawska-Serda, M.; Nguyen, L.; Law, J.; Anderson, A.O.; Curley, S.A.; Wilson, L.J.; et al. Development of photoactive Sweet-C60 for pancreatic cancer stellate cell therapy. *Nanomedicine* **2018**, *13*, 2981–2993. [CrossRef]

23. Ashcroft, J.M.; Tsyboulski, D.A.; Hartman, K.B.; Zakharian, T.Y.; Marks, J.W.; Weisman, R.B.; Rosenblum, M.G.; Wilson, L.J. Fullerene (C60) immunoconjugates: Interaction of water-soluble C60 derivatives with the murine anti-gp240 melanoma antibody. *Chem. Commun.* **2006**, *28*, 3004–3006. [CrossRef] [PubMed]

24. Fan, J.; Fang, G.; Zeng, F.; Wang, X.; Wu, S. Water-Dispersible Fullerene Aggregates as a Targeted Anticancer Prodrug with both Chemo- and Photodynamic Therapeutic Actions. *Small* **2013**, *9*, 613–621. [CrossRef] [PubMed]

25. Cagle, D.W.; Kennel, S.J.; Mirzadeh, S.; Alford, J.M.; Wilson, L.J. In vivo studies of fullerene-based materials using endohedral metallofullerene radiotracers. *Proc. Natl. Acad. Sci. USA* **1999**, *96*, 5182–5187. [CrossRef] [PubMed]

26. Yamago, S.; Tokuyama, H.; Nakamura, E.; Kikuchi, K.; Kananishi, S.; Sueki, K.; Nakahara, H.; Enomoto, S.; Ambe, F. In vivo biological behavior of a water-miscible fullerene: 14C labeling, absorption, distribution, excretion and acute toxicity. *Chem. Biol.* **1995**, *2*, 385–389. [CrossRef]

27. Wharton, T.; Wilson, L.J. Highly-Iodinated Fullerene as a Contrast Agent for X-ray Imaging. *Bioorganic Med. Chem.* **2002**, *10*, 3545–3554. [CrossRef]

28. Chaudhuri, P.; Paraskar, A.; Soni, S.; Mashelkar, R.A.; Sengupta, S. Fullerenol–Cytotoxic Conjugates for Cancer Chemotherapy. *ACS Nano* **2009**, *3*, 2505–2514. [CrossRef]

29. Sigwalt, D.; Holler, M.; Iehl, J.; Nierengarten, J.-F.; Nothisen, M.; Morin, E.; Remy, J.-S. Gene delivery with polycationic fullerene hexakis-adducts. *Chem. Commun.* **2011**, *47*, 4640–4642. [CrossRef]

30. Isobe, H.; Nakanishi, W.; Tomita, N.; Jinno, S.; Okayama, H.; Nakamura, E. Nonviral Gene Delivery by Tetraamino Fullerene. *Mol. Pharm.* **2006**, *3*, 124–134. [CrossRef]

31. Zakharian, T.Y.; Seryshev, A.; Sitharaman, B.; Gilbert, B.E.; Knight, V.; Wilson, L.J. A Fullerene−Paclitaxel Chemotherapeutic: Synthesis, Characterization, and Study of Biological Activity in Tissue Culture. *J. Am. Chem. Soc.* **2005**, *127*, 12508–12509. [CrossRef]

32. Lusic, H.; Grinstaff, M.W. X-ray-Computed Tomography Contrast Agents. *Chem. Rev.* **2013**, *113*, 1641–1666. [CrossRef]

33. Wharton, T.; Kini, V.U.; Mortis, R.A.; Wilson, L.J. New non-ionic, highly water-soluble derivatives of C60 designed for biological compatibility. *Tetrahedron Lett.* **2001**, *42*, 5159–5162. [CrossRef]

34. Raoof, M.; Mackeyev, Y.; Cheney, M.A.; Wilson, L.J.; Curley, S.A. Internalization of C60 fullerenes into cancer cells with accumulation in the nucleus via the nuclear pore complex. *Biomaterials* **2012**, *33*, 2952–2960. [CrossRef] [PubMed]

35. Hirsch, A.; Vostrowsky, O. C60 hexakisadducts with an octahedral addition pattern − a new structure motif in organic chemistry. *Eur. J. Org. Chem.* **2001**, *2001*, 829–848. [CrossRef]

36. Sitharaman, B.; Zakharian, T.Y.; Saraf, A.; Misra, P.; Ashcroft, J.; Pan, S.; Pham, Q.P.; Mikos, A.G.; Wilson, L.J.; Engler, D.A. Water-Soluble Fullerene (C60) Derivatives as Nonviral Gene-Delivery Vectors. *Mol. Pharm.* **2008**, *5*, 567–578. [CrossRef] [PubMed]

37. Mackeyev, Y.; Raoof, M.; Cisneros, B.T.; Koshkina, N.V.; Berger, C.; Wilson, L.J.; Curley, S.A. Toward Paclitaxel-[60]Fullerene Immunoconjugates as a Targeted Prodrug Against Cancer. In Proceedings of the Nanosystems: Physics, Chemistry, Mathematics, St. Petersburg, Russia, 1–5 July 2013; St. Petersburg National Research University of Information Technologies, Mechanics, and Optics: St. Petersburg, Russia, 2014; pp. 67–75.

38. Li, J.; Yang, W.; Cui, R.; Wang, D.; Chang, Y.; Gu, W.; Yin, W.; Bai, X.; Chen, K.; Xia, L.; et al. Metabolizer in vivo of fullerenes and metallofullerenes by positron emission tomography. *Nanotechnology* **2016**, *27*, 155101. [CrossRef]

39. Peng, Y.; Yang, D.; Lu, W.; Hu, X.; Hong, H.; Cai, T. Positron emission tomography (PET) guided glioblastoma targeting by a fullerene-based nanoplatform with fast renal clearance. *Acta Biomater.* **2017**, *61*, 193–203. [CrossRef]

40. Hardt, J.I.; Perlmutter, J.S.; Smith, C.J.; Quick, K.L.; Wei, L.; Chakraborty, S.K.; Dugan, L.L. Pharmacokinetics and Toxicology of the Neuroprotective e,e,e-Methanofullerene(60)-63-tris Malonic Acid [C3] in Mice and Primates. *Eur. J. Drug Metab. Pharmacokinet.* **2018**, *43*, 543–554. [CrossRef] [PubMed]

41. Wang, C.; Bai, Y.; Li, H.; Liao, R.; Li, J.; Zhang, H.; Zhang, X.; Zhang, S.; Yang, S.-T.; Chang, X.-L. Surface modification-mediated biodistribution of ^{13}C-fullerene $C_6$0 in vivo. *Part Fibre Toxicol.* **2016**, *13*, 14–28. [CrossRef] [PubMed]

42. Zeglis, B.M.; Lewis, J.S. A practical guide to the construction of radiometallated bioconjugates for positron emission tomography. *Dalton Trans.* **2011**, *40*, 6168–6195. [CrossRef]

43. Shokeen, M.; Anderson, C.J. Molecular Imaging of Cancer with Copper-64 Radiopharmaceuticals and Positron Emission Tomography (PET). *Acc. Chem. Res.* **2009**, *42*, 832–841. [CrossRef]

44. Dumont, R.A.; Deininger, F.; Haubner, R.; Maecke, H.R.; Weber, W.A.; Fani, M. Novel 64Cu- and 68Ga-Labeled RGD Conjugates Show Improved PET Imaging of αvβ3 Integrin Expression and Facile Radiosynthesis. *J. Nucl. Med.* **2011**, *52*, 1276–1284. [CrossRef] [PubMed]

45. Roeper, J.R.; Elias, H. Kinetic studies of nickel(II) and copper(II) complexes with N4 macrocycles of the cyclam type. 1. Kinetics and mechanism of complex formation with different N-methylated 1,4,8,11-tetraazacyclotetradecanes. *Inorg. Chem.* **1992**, *31*, 1202–1210. [CrossRef]

46. Zarschler, K.; Kubeil, M.; Stephan, H. Establishment of two complementary in vitro assays for radiocopper complexes achieving reliable and comparable evaluation of in vivo stability. *RSC Adv.* **2014**, *4*, 10157–10164. [CrossRef]

47. Lapin, N.A.; Vergara, L.A.; Mackeyev, Y.; Newton, J.M.; Dilliard, S.A.; Wilson, L.J.; Curley, S.A.; Serda, R.E. Biotransport kinetics and intratumoral biodistribution of malonodiserinolamide-derivatized [60]fullerene in a murine model of breast adenocarcinoma. *Int. J. Nanomed.* **2017**, *12*, 8289–8307. [CrossRef] [PubMed]

48. Ghosh, S.C.; Pinkston, K.L.; Robinson, H.; Harvey, B.R.; Wilganowski, N.; Gore, K.; Sevick-Muraca, E.M.; Azhdarinia, A. Comparison of DOTA and NODAGA as chelators for 64Cu-labeled immunoconjugates. *Nucl. Med. Biol.* **2015**, *42*, 177–183. [CrossRef]

49. He, C.; Hu, Y.; Yin, L.; Tang, C.; Yin, C. Effects of particle size and surface charge on cellular uptake and biodistribution of polymeric nanoparticles. *Biomaterials* **2010**, *31*, 3657–3666. [CrossRef]

50. Cheney, M.A. Radiofrequency-Induced Cellular Hyperthermia: Water-Soluble Fullerene as a New Cancer Therapeutic Agent. Ph.D. Thesis, Rice University, Houston, TX, USA, 2014.

51. Jones-Wilson, T.M.; Deal, K.A.; Anderson, C.J.; McCarthy, D.W.; Kovacs, Z.; Motekaitis, R.J.; Sherry, A.D.; Martell, A.E.; Welch, M.J. The in vivo behavior of copper-64-labeled azamacrocyclic complexes. *Nucl. Med. Biol.* **1998**, *25*, 523–530. [CrossRef]

52. Cisneros, B.T.; Law, J.J.; Matson, M.L.; Azhdarinia, A.; Sevick-Muraca, E.M.; Wilson, L.J. Stable confinement of positron emission tomography and magnetic resonance agents within carbon nanotubes for bimodal imaging. *Nanomed. UK* **2014**, *9*, 2499–2509. [CrossRef]

53. Sun, X.; Huang, X.; Yan, X.; Wang, Y.; Guo, J.; Jacobson, O.; Liu, D.; Szajek, L.P.; Zhu, W.; Niu, G.; et al. Chelator-Free 64Cu-Integrated Gold Nanomaterials for Positron Emission Tomography Imaging Guided Photothermal Cancer Therapy. *ACS Nano* **2014**, *8*, 8438–8446. [CrossRef]

54. Chen, F.; Hong, H.; Shi, S.; Goel, S.; Valdovinos, H.F.; Hernandez, R.; Theuer, C.P.; Barnhart, T.E.; Cai, W. Engineering of Hollow Mesoporous Silica Nanoparticles for Remarkably Enhanced Tumor Active Targeting Efficacy. *Sci. Rep.* **2014**, *4*, 5080. [CrossRef]

55. Aggarwal, P.; Hall, J.B.; McLeland, C.B.; Dobrovolskaia, M.A.; McNeil, S.E. Nanoparticle interaction with plasma proteins as it relates to particle biodistribution, biocompatibility and therapeutic efficacy. *Adv. Drug Deliv. Rev.* **2009**, *61*, 428–437. [CrossRef] [PubMed]

56. Johnston, H.J.; Hutchison, G.R.; Christensen, F.M.; Aschberger, K.; Stone, V. The Biological Mechanisms and Physicochemical Characteristics Responsible for Driving Fullerene Toxicity. *Toxicol. Sci.* **2010**, *114*, 162–182. [CrossRef] [PubMed]

57. Almeida, J.P.M.; Chen, A.L.; Foster, A.; Drezek, R. In vivo biodistribution of nanoparticles. *Nanomedicine* **2011**, *6*, 815–835. [CrossRef] [PubMed]

58. Qingnuan, L.; Yan, X.; Xiaodong, Z.; Ruili, L.; Qieqie, D.; Xiaoguang, S.; Shaoliang, C.; Wenxin, L. Preparation of 99mTc-C60(OH)x and its biodistribution studies. *Nucl. Med. Biol.* **2002**, *29*, 707–710. [CrossRef]

59. Ji, Z.Q.; Sun, H.; Wang, H.; Xie, Q.; Liu, Y.; Wang, Z. Biodistribution and tumor uptake of C60(OH)xin mice. *J. Nanopart. Res.* **2006**, *8*, 53–63. [CrossRef]

60. Rajagopalan, P.; Wudl, F.; Schinazi, R.F.; Boudinot, F.D. Pharmacokinetics of a water-soluble fullerene in rats. *Antimicrob. Agents Chemother.* **1996**, *40*, 2262–2265. [CrossRef]

61. Riviere, J.E. Pharmacokinetics of nanomaterials: An overview of carbon nanotubes, fullerenes and quantum dots: Pharmacokinetics of nanomaterials. *Wiley Interdiscip. Rev. Nanomed. Nanobiotechnol.* **2009**, *1*, 26–34. [CrossRef]

62. Misra, C.; Kumar, M.; Sharma, G.; Kumar, R.; Singh, B.; Katare, O.P.; Raza, K. Glycinated fullerenes for tamoxifen intracellular delivery with improved anticancer activity and pharmacokinetics. *Nanomedicine (Lond.)* **2017**, *12*, 1011–1023. [CrossRef]

63. Kumar, M.; Sharma, G.; Kumar, R.; Singh, B.; Katare, O.P.; Raza, K. Lysine-Based C60-Fullerene Nanoconjugates for Monomethyl Fumarate Delivery: A Novel Nanomedicine for Brain Cancer Cells. *ACS Biomater. Sci. Eng.* **2018**, *4*, 2134–2142. [CrossRef]

64. Raza, K.; Thotakura, N.; Kumar, P.; Joshi, M.; Bhushan, S.; Bhatia, A.; Kumar, V.; Malik, R.; Sharma, G.; Guru, S.K.; et al. C60-fullerenes for delivery of docetaxel to breast cancer cells: A promising approach for enhanced efficacy and better pharmacokinetic profile. *Int. J. Pharm.* **2015**, *495*, 551–559. [CrossRef]

65. Sheka, E. *Fullerenes: Nanochemistry, Nanomagnetism, Nanomedicine, Nanophotonics*; CRC Press: Boca Raton, FL, USA, 2011; ISBN 978-1-4398-0643-2.

66. Shi, J.; Liu, Y.; Wang, L.; Gao, J.; Zhang, J.; Yu, X.; Ma, R.; Liu, R.; Zhang, Z. A tumoral acidic pH-responsive drug delivery system based on a novel photosensitizer (fullerene) for in vitro and in vivo chemo-photodynamic therapy. *Acta Biomater.* **2014**, *10*, 1280–1291. [CrossRef] [PubMed]